The EMBO Journal (2011) 30, 2734–2747 | © 2011 European Molecular Biology Organization | Some Rights Reserved 0261-4189/11
www.embojournal.org

THE EMBO JOURNAL

EMBO open

Structural basis of cargo recognition by the myosin-X MyTH4–FERM domain

Yoshinori Hirano[1], Taiki Hatano[1], Aya Takahashi[1], Michinori Toriyama[2], Naoyuki Inagaki[2] and Toshio Hakoshima[1,*]

[1]Structural Biology Laboratory, Nara Institute of Science and Technology, Nara, Japan and [2]Signal Transduction Laboratories, Graduate School of Biological Sciences, Nara Institute of Science and Technology, Nara, Japan

Myosin-X is an important unconventional myosin that is critical for cargo transportation to filopodia tips and is also utilized in spindle assembly by interacting with microtubules. We present a series of structural and biochemical studies of the myosin-X tail domain cassette, consisting of myosin tail homology 4 (MyTH4) and FERM domains in complex with its specific cargo, a netrin receptor DCC (deleted in colorectal cancer). The MyTH4 domain is folded into a helical VHS-like structure and is associated with the FERM domain. We found an unexpected binding mode of the DCC peptide to the subdomain C groove of the FERM domain, which is distinct from previously reported β–β associations found in radixin–adhesion molecule complexes. We also revealed direct interactions between the MyTH4–FERM cassette and tubulin C-terminal acidic tails, and identified a positively charged patch of the MyTH4 domain, which is involved in tubulin binding. We demonstrated that both DCC and integrin bindings interfere with microtubule binding and that DCC binding interferes with integrin binding. Our results provide the molecular basis by which myosin-X facilitates alternative dual binding to cargos and microtubules.

The EMBO Journal (2011) **30,** 2734–2747. doi:10.1038/emboj.2011.177; Published online 3 June 2011
Subject Categories: membranes & transport; cell & tissue architecture; structural biology
Keywords: DCC; integrin; microtubule; unconventional myosin; X ray crystallography

Introduction

A large number of unconventional myosins appeared early in eukaryotic evolution and these have vital roles in diverse cellular processes including intracellular transport, organization of F-actin, mitotic spindle regulation and gene transcription (Berg *et al*, 2001; Richards and Cavalier-Smith, 2005; Foth *et al*, 2006; Woolner and Bement, 2009). Myosins consist of three distinct regions, a head, neck and tail. The heads contain actin-based motor domains that display homology among different myosins and these structures have been extensively studied (O'Connell *et al*, 2007). In sharp contrast to the motor domains, the tails display diversity by combination of a variety of functional domains that mediate cargo recognition, which determine the individual cellular functions of myosins. However, little is known about the tail domain structures and their specific cargo recognition.

Myosin-X (Myo-X, myosin-10, Myo10) is an unconventional myosin implicated in elongation of filopodia, which function as tentacles that explore and interact with cell surroundings to determine the direction of cell movement and to establish cell adhesion such as in the case of synapses (Sousa and Cheney, 2005). Myosin-X is localized at filopodia tips containing a 'filopodial-tip complex', which act as fingertips and sensors in processes such as signal perception, cell signalling, actin polymerization inside of filopodia and adhesion (Berg *et al*, 2000; Berg and Cheney, 2002). Elucidating the molecular nature of the filopodial-tip complex is key for understanding filopodia functions, but has remained a mystery for over 30 years. The manner by which myosin-X discriminates between cargos for transportation to the tip and how these cargos contribute to filopodial processes at the tip remains unknown. Myosin-X contains myosin tail homology 4 (MyTH4) and 4.1 and ezrin/radixin/moesin (FERM) domains for cargo recognition (Figure 1A). The tandem comprising the MyTH4 and FERM domains frequently appears in related myosins (myosin-IV, VII, X, XII, XIV and XV), and is referred to as the MyTH4–FERM cassette. Interestingly, this cassette is found in one of three ancestral myosins in the earliest eukaryotes, and myosin-X is conserved in vertebrates (Richards and Cavalier-Smith, 2005).

One of the most exciting processes involving myosin-X relates to the axon pathfinding of neurons, which is essential for proper wiring in the brain. During neural development, axons are navigated by extracellular guidance cues such as those provided by netrins. Deleted in colorectal cancer (DCC) and neogenin are membrane proteins that function as netrin receptors (Chan *et al*, 1996; Keino-Masu *et al*, 1996; Kolodziej *et al*, 1996). Myosin-X recognizes these receptors as cargos and redistributes to the cell periphery or to the tips of neurites, where growth cones dynamically develop filopodia (Zhu *et al*, 2007). Moreover, of particular interest is that myosin-X interacts with integrin through its FERM domain and mediates relocalization of integrin to filopodial tips and thereby promotes filopodial extension by serving to form adhesive structures (Zhang *et al*, 2004). A very recent report has shown that DCC is also important as a cargo adaptor that

*Corresponding author. Structural Biology Laboratory, Nara Institute of Science and Technology, 8916-5 Takayama, Ikoma, Nara 630-0192, Japan. Tel.: +81 74 372 5570; Fax: +81 74 372 5579;
E-mail: hakosima@bs.naist.jp

Received: 8 February 2011; accepted: 6 May 2011; published online: 3 June 2011

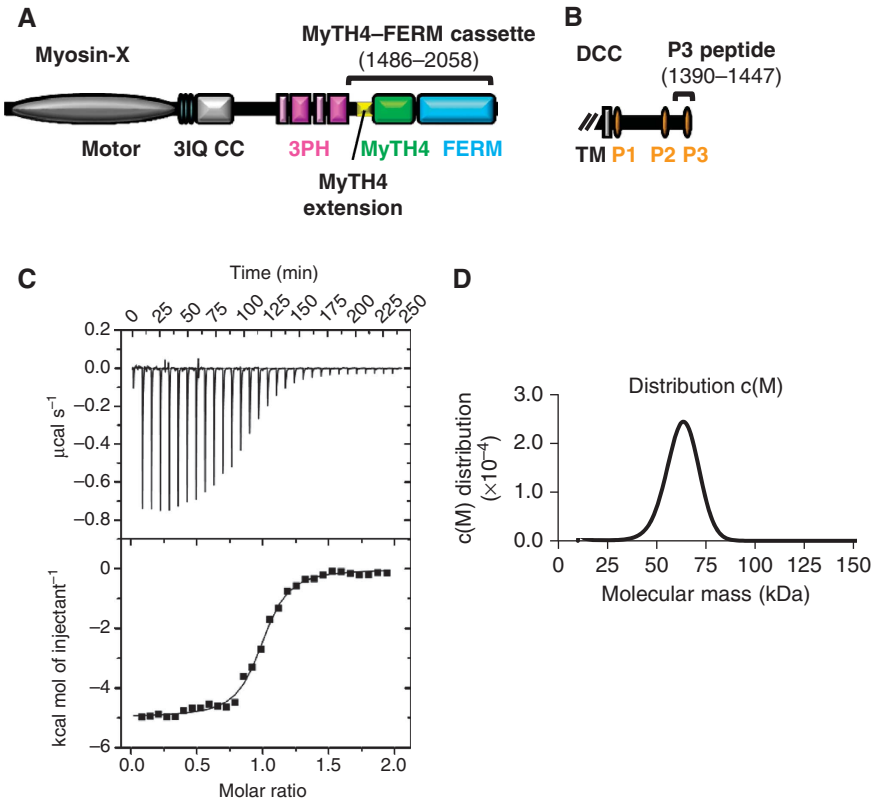

Figure 1 Diagrams of domains and motifs found in myosin-X and DCC and their physical properties. (**A**) Myosin-X consists of an N-terminal motor domain, three IQ motifs, a coiled-coil (CC) region, three PH domains and MyTH4 and FERM domains. The tandem MyTH4 and FERM domain cassette has a central role in cargo recognition. Three PH domains contain one split PH domain (PHn and PHc) and sequentially appear as PHn–PH1–PHc–PH2. (**B**) The DCC cytoplasmic tail possesses three conserved regions, P1, P2 and P3 (orange ovals), which might facilitate protein–protein interactions. The transmembrane helix (TH) is represented by a grey rectangle. (**C**) ITC profiles and thermodynamic data for binding experiments at 20°C. Injections of 6 µl of 733 µM DCC peptide into 50 µM MyTH4–FERM cassette solution. The protein exhibited a K_D value of 0.53 ± 0.06 µM, ΔH of −4.98 ± 0.04 kcal/mol and ΔS of 11.7 cal/mol. Raw data for 30 sequential injections (the upper panel) and the plot of the heat evolved (kcal) per mole of DCC peptide added, corrected for the heat of the peptide dilution, against the molar ratio of the peptide to the cassette. The data (filled squares) were fitted using the software 'one set of sites', and the solid line represents the best fit. (**D**) Hydrodynamic property of the complex determined by AUC measurements. The distribution of apparent molecular mass obtained from sedimentation velocity analysis of the complex shows a mono-modal peak with apparent molecular mass of 62.7 ± 8.6 kDa.

mediates local translation events in neurons by anchoring components of the translational machinery such as ribosome subunits at the plasma membrane of growth cones and dendrites (Tcherkezian *et al*, 2010).

In addition to mediating the biological function of selective cargo transportation on actin cables, myosin-X directly interacts with microtubules and has a key role in spindle assembly during meiosis to ensure faithful delivery of replicated chromosomes to daughter cells following cell division (Weber *et al*, 2004; Woolner *et al*, 2008). This surprising myosin-X function is mediated by a direct interaction between microtubules and the MyTH4–FERM cassette. However, the manner by which myosin-X recognizes microtubules has remained unclear. Interestingly, myosin-X has a role in integrin-dependent spindle orientation (Toyoshima and Nishida, 2007).

Here, we report on a series of structural and biochemical/biophysical studies concerning DCC recognition by the myosin-X MyTH4–FERM cassette. We reveal the presence of a VHS-like fold within the MyTH4 domain. Our 1.9 Å resolution structure clarifies details of an unexpected binding mode of DCC to the myosin-X FERM domain, which is distinct from those found in the FERM domain of radixin that links membrane protein/plasma membrane and actin cytoskeletons. We also show that the cassette binds the C-terminal acidic tails of tubulins and that this binding is obstructed by DCC binding. Moreover, we show that the cassette binds the cytoplasmic tail of the integrin β5-subunit and that this binding is obstructed by DCC binding. Like DCC, integrin β5 binding also interferes with microtubule binding. Our results reveal the structural mechanism that underlies cargo recognition by the cassette and provide the molecular basis for further structural and functional investigations of biologically and medically important myosin-X, as well as of the related unconventional myosins containing MyTH4–FERM cassette.

Results

Preparation of proteins and binding assay

DCC possesses a long (~340 residues) cytoplasmic tail that contains three highly conserved regions designated as P1, P2 and P3 (Kolodziej *et al*, 1996) (Figure 1B). C-terminal regions containing the P3 region (residues 1424–1447) were shown to bind myosin-X by a two-hybrid system binding assay, and the MyTH4–FERM cassette was found to be sufficient for DCC and neogenin binding (Zhu *et al*, 2007). We prepared a peptide encompassing the C-terminal 58

residues (1390–1447) of human DCC for our studies, hereafter referred to as the DCC P3 peptide.

We performed the screening of protein expression constructs of human myosin-X and found that a construct encoding 573 residues (1486–2058) containing the MyTH4–FERM cassette expressed a soluble protein in bacteria, although the protein has propensity for degradation during purification. We set out to find a major degradation site(s) in our sample and identified two fragments, Frag-1 (~48 kDa) and Frag-2 (~18 kDa), which appeared at an early stage of the purification (Supplementary Figure S1A, inset). Our TOF-MS spectra and N-terminal analysis suggested that these fragments correspond to two halves produced from the full-length cassette (66 kDa), and that Frag-1 encompasses residues 1486–1888 and Frag-2 the C-terminal 156 residues from Phe1893 (Supplementary Figure S1A). We found that the myosin-X FERM domain contains a poorly conserved insertion spanning residues 1851–1917 when compared with a prototypic FERM domain such as the radixin FERM domain, whose structure is well established (Hamada *et al*, 2000, 2003) (Supplementary Figure S2). We observed that Frag-1 and Frag-2 were co-purified and still able to bind the DCC P3 peptide. Since these data implied that the insertion was not critical, we attempted to suppress degradation by modifying the insertion. We found that our deletion constructs yielded proteins, which were not degraded during the purification and had their binding affinity to the DCC P3 peptide preserved (Supplementary Figure S1B). For the present structural study, we used the construct containing the Δ20 deletion (residues 1872–1891). We also used this construct, referred to as the MyTH4–FERM cassette, in further biochemical studies. Isothermal titration calorimetry (ITC) showed a relatively strong affinity with a dissociation constant K_D value of 0.53 μM (Figure 1C).

The purified myosin-X MyTH4–FERM cassette exists as a monomer in solution as suggested by analytical ultracentrifugation (AUC) analysis, which showed a mono-modal peak corresponding to a monomer (62.7 kDa) close to the calculated (63.3 kDa) (Figure 1D). Our MyTH4–FERM cassette and the DCC P3 peptide form a stable complex, which could be purified using conventional gel filtration. Gel filtration and AUC showed a mono-modal peak corresponding to a 1:1 complex (data not shown). Contrary to the cargo-loaded dimerization of myosin VI (Yu *et al*, 2009), no cargo-mediated dimerization was observed for myosin-X through the MyTH4–FERM cassette.

Structure determination and overall structure

The crystal structure of the complex between the myosin-X MyTH4–FERM cassette and the DCC C-terminal P3 peptide was determined by single-wavelength anomalous dispersion (SAD) methods and was refined to 1.9 Å resolution. The current model contains 524 residues (1501–2046) of the MyTH4–FERM cassette and 32 residues (1414–1445) of the DCC P3 peptide encompassing the conserved P3 region: 15 N- and 12 C-terminal residues of the cassette and 24 N- and 2 C-terminal residues of the DCC peptide were not observed in the current map. The free form structure of the MyTH4–FERM cassette was determined by the molecular replacement method using the cassette model of the complex structure and refined at 2.55 Å.

The myosin-X MyTH4–FERM cassette displays a rather elongated shape with multiple globular domains. The overall fold of the FERM domain is preserved, comprising three subdomains A, B and C (also referred to as F1, F2 and F3 lobes), which display a ubiquitin fold, a helix bundle and a PTB-like fold, respectively, as observed in the FERM domains of ERM proteins (Hamada *et al*, 2000; Pearson *et al*, 2000) (Figure 2A). The MyTH4 domain is a globular domain comprising α-helices and sits on subdomain A of the FERM domain without direct contacts with subdomain B or C. Our MyTH4–FERM cassette construct contains the linker region (residues 1488–1556) between the upstream PH domain and the MyTH4 domain (Figure 1A). Excepting its N-terminal 13 residues, this linker region is well defined in our map and forms two α-helices (α1x and α2x) and one short 3_{10} helix (ηx). We refer to this linker as the MyTH4 extension (MyTH4 Ex), which is closely associated with the MyTH4 domain. The DCC P3 peptide forms two helices, one shorter N-terminal α-helix (αP3′) followed by a longer 5-turn α-helix (αP3), and binds subdomain C of the FERM domain.

MyTH4 domain is folded into a VHS-like structure

The myosin-X MyTH4 domain forms a helix bundle structure containing eight α-helices (α1′M, α1M–α4M, α6M–α8M), which resembles the Vps27p/Hrs/STAM (VHS) domain composed of ~140 residues that mediates protein–protein interactions (Mao *et al*, 2000) (Figure 2A). VHS domains belong to the superfamily of superhelical structures including HEAT and armadillo (ARM) repeat domains and are generally found at the very N-terminus of adaptor proteins that participate in vesicular trafficking (Lohi *et al*, 2002), whereas MyTH4 domains are found in the middle of proteins. Our MyTH4 domain superimposed upon VHS domains with root-mean-squares (r.m.s.) deviations of <3 Å, although the sequence identity is extremely poor (~10%). Typical VHS domains have eight conserved α-helices (α1–α8) forming a right-handed superhelix, and six of these overlapped well with the MyTH4 helices (Figure 2C).

The most prominent difference between the MyTH4 and VHS domains is found in the last α8M helix, which is displaced from the groove between α6M and α7M helices to the groove between α2M and α4M helices (indicated with an arrow in Figure 2C), and has a key role in formation of the interface with the FERM domain (Figure 2A). Additionally, the MyTH4 domain lacks the VHS α5 helix, but has an additional N-terminal α1′M helix. The displacement of α8M contrasts the MyTH4 and VHS domain functions. First, the VHS domains of Golgi-localization/γ-ear-containing/ADP-ribosylation-factor-binding (GGA) adaptor proteins provide the groove formed by α6 and α8 helices for binding of the acidic-cluster dileucine sorting signals to the compartments of the endosomal–lysosomal system (Misra *et al*, 2002; Shiba *et al*, 2002), whereas the MyTH4 domain lacks the groove due to the displacement of α8M. Second, the VHS domain of STAM has the ubiquitin-binding surface formed by α2 and α4 helices (Mizuno *et al*, 2003; Ren and Hurley, 2010), whereas the corresponding surface of the MyTH4 domain is occupied by the displaced α8M helix. The MyTH4 extension comprising α1x and α2x helices are packed on the surface formed by α1M, α3M and α6M helices, which seems to interfere with the binding of GGA VHS domains to the acidic-cluster dileucine sorting signals (Figure 2C).

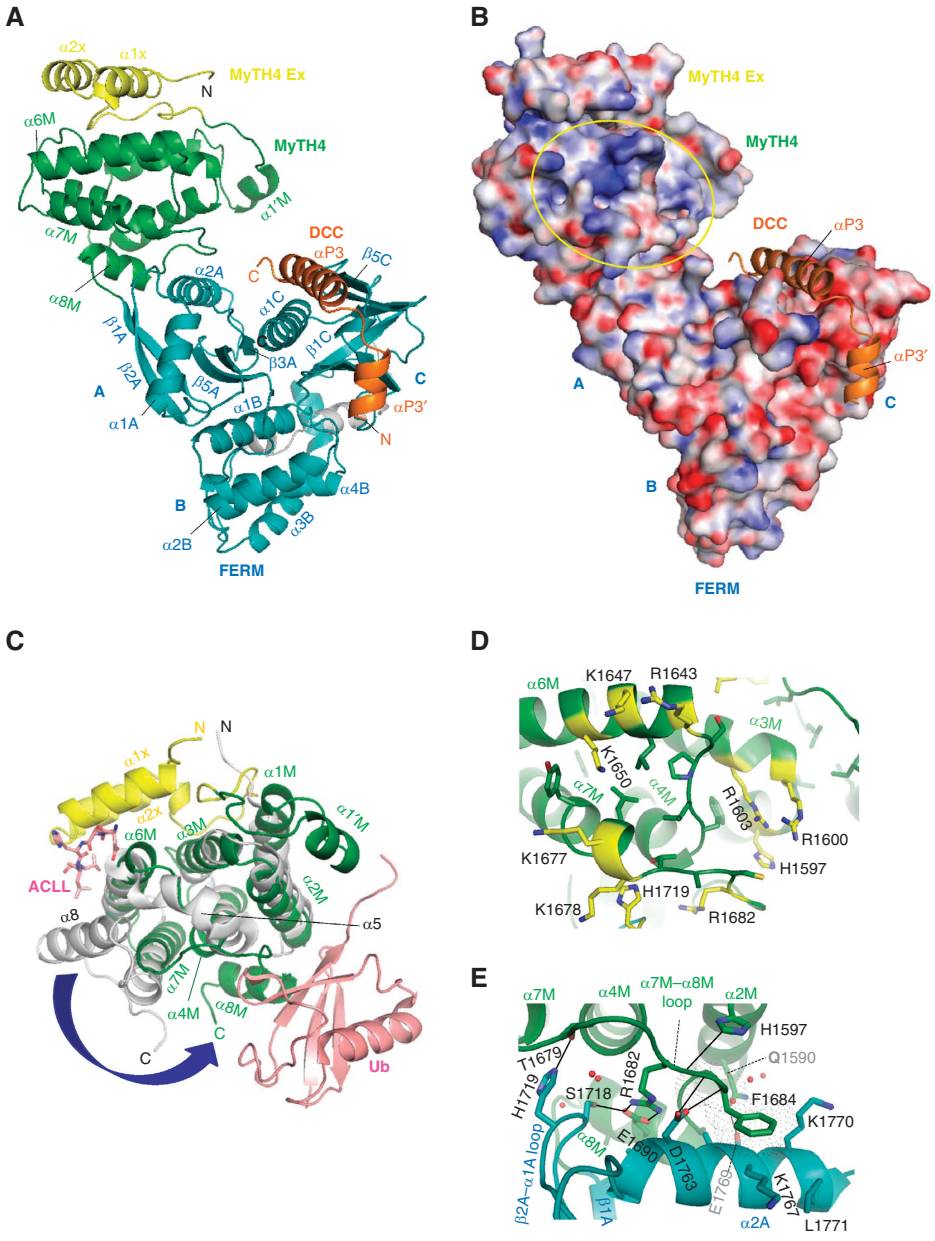

Figure 2 Overall structure of the complex between the myosin-X MyTH4–FERM cassette and the DCC P3 peptide. (**A**) Ribbon representation of the myosin-X MyTH4–FERM–DCC P3 complex. The MyTH4–FERM cassette contains the MyTH4 extension (yellow), and MyTH4 (green) and FERM (cyan) domains. The FERM domain consists of subdomains A, B and C. The DCC P3 peptide (orange) binds subdomain C. (**B**) Electrostatic surface potentials of the myosin-X MyTH4–FERM cassette. The electrostatic surface potentials are shaded blue in positively and red in negatively charged regions, respectively. The bound DCC P3 peptide is shown as a ribbon model (orange). The yellow oval indicates the positively charged patch, which was identified as the microtubule-binding site in this study. (**C**) Comparison of MyTH4 and VHS domains. The myosin-X MyTH4 domain (green) superimposed on the STAM2 VHS domain (grey) bound to ubiquitin (Ub, pink) (3LDZ). Six helices (α1–α4, α6–α7) out of the eight conserved helices of the VHS domain are overlapped with corresponding helices. The MyTH4 domain lacks the α5 helix of the VHS domain. A large flipping over of the α8M helix of the MyTH4 domain relative to the corresponding α8 helix of the VHS domain is indicated with a blue arrow. The acidic-cluster dileucine sorting signal peptide (ACLL, pink) of the cation-dependent mannose-6-phosphate receptor bound to the GGA3 VHS domain (1JUQ) is modelled on the STAM VHS domain structure to show the peptide-binding site. (**D**) The positively charged patch on the MyTH4 domain. A cluster of basic residues (yellow) surrounds nonpolar residues. The basic residues include the C-terminal part of the α2M helix (His1597) and the N-terminal part of α3M helix (Arg1600 and Arg1603), the N-terminal part of the α6M helix (Arg1643, Lys1647 and Lys1650), the C-terminal part of the α7M helix and the flanking loop (Lys1677, Lys1678 and Arg1682). (**E**) The interface between the MyTH4 and FERM domains. The short linker between the α8M helix and β1A strand links the MyTH4 (green) and FERM (cyan) domains. The interface involves the α7M–α8M loop and α8M helix from the MyTH4 domain and the β2A–α1A loop and α2A helix from subdomain A.

It should be noted that the MyTH4 domain possesses a positively charged patch on the domain surface facing the FERM domain (indicated with an yellow oval in Figure 2B). This patch, which will be examined for a microtubule-binding site below, contains several Arg and Lys residues from α2M–α3M and α6M–α7M helices and connecting loops surrounding nonpolar residues (Figure 2D).

In summary, the MyTH4 domain is folded into a VHS domain-like structure but possesses unique molecular surfaces formed by the rearrangement of helices and the

presence of a charged surface patch, which probably serve as a protein–protein recognition site distinct from that of VHS domains.

FERM domain structure

The myosin-X FERM domain is distantly related to the prototype FERM domains found in ERM proteins with low (~20%) sequence identity. This poor homology is reflected in the structural deviations from the prototype FERM domains (Hamada *et al*, 2000; Pearson *et al*, 2000; Edwards and Keep, 2001; Shimizu *et al*, 2002; Smith *et al*, 2003). The closest structural match to the myosin-X FERM domain occurs in the radixin FERM domain, whose subdomain A, B or C superimposes with the corresponding subdomains (r.m.s. deviations of 2.3, 2.1 or 1.4 Å, respectively) (Supplementary Figure S3A). Compared with the radixin FERM domain, a 10-residue insertion exists between the β4A and β5A strands of subdomain A, and results in a longer α2A helix, which has a central role in forming the interface with the MyTH4 domain. Subdomain B also contains a long insertion (41 residues), of which 20 C-terminal residues are deleted in the current construct as mentioned above. The insertion exists between α2B and α3B helices and forms two additional helices (α2′iB and α2″iB) followed by a long loop. These inserted elements are remote from the DCC-binding site. In contrast to subdomains A and B, subdomain C has no additional insertion but exhibits a change in orientation relative to subdomains A and B with an ~10° rotation, such that the C-terminal end of α1C helix is lifted up away from subdomain B (Supplementary Figure S3B). The shift is induced by changes in nonpolar side-chain packing at the inter-subdomain interfaces (Supplementary Figure S3C and D).

FERM domains of ERM proteins form a positively charged cleft between subdomains A and C, which is involved in binding to phosphatidylinositol 4,5-bisphosphate (PtdIns(4,5)P_2), and is essential for localization and activation of ERM proteins in cells (Hamada *et al*, 2000). The myosin-X FERM domain does not possess this positively charged cleft and lacks the conserved PtdIns(4,5)P_2-interacting residues (radixin Lys60, Asn62, Lys63 and Lys278) (Figure 2B; Supplementary Figure S2). Myosin-X interacts with PI3K products such as PtdIns(3,4,5)P_3 through the second PH domain of the PH domain cluster rather than the FERM domain (Isakoff *et al*, 1998).

The interface between the MyTH4 and FERM domains

The myosin-X MyTH4–FERM cassette displays a close association between the MyTH4 domain and subdomain A of the FERM domain with the interface that buries the total accessible surface area of 1117 Å^2, comprising the α8M helix and α7M–α8M loop of the MyTH4 domain and the long α2A helix of FERM subdomain A (Figure 2A). These secondary structural elements are unique to myosin-X MyTH4 and FERM domains as mentioned above. The conformation of the α7M–α8M loop is stabilized by a salt bridge between Arg1682 and Glu1690 inside the loop, enabling polar and nonpolar contacts with the α2A helix (Figure 2E). The tight association between MyTH4 and FERM domains was implied by the short inter-domain linker comprising a few residues, suggesting a similar tight inter-domain association of MyTH4–FERM cassettes of related myosins VII, XII and XV.

Myosin-X–DCC interactions

The DCC P3 peptide forms two α-helices, αP3′ and αP3, linked by three residues and kinked by ~90° (Figure 2A). The longer αP3 helix almost encompasses the previously suggested P3 region (Kolodziej *et al*, 1996) and is docked into the hydrophobic groove between β5C strand and α1C helix of FERM subdomain C (Figure 3A and B). No direct interaction was observed with subdomains A and B or with the MyTH4 domain. The observed DCC binding to subdomain C in our crystal was supported by the *in vivo* binding assay, which showed co-immunoprecipitation of DCC with myc-tagged myosin-X MyTH4–FERM cassette, indicating a DCC–MyTH4–FERM interaction in HEK239T cells, but no interaction with the MyTH4–FERM cassette lacking subdomain C, myc–MyTH4–FERM(ΔC) (Figure 3C).

In our structure, the αP3 helix runs in an anti-parallel direction against the α1C helix of subdomain C, with the helical axis inclined by ~20° and allowing nonpolar residues to fill up this groove (Figure 2A). Of these nonpolar residues, three Leu residues (Leu1425, Leu1432 and Leu1439) occupy the heptad position of the helix and, together with five nonpolar residues (Met1429, Leu1435–Met1436 and Ile1442–Thr1443) at the off-heptad positions, are packed into the groove in a knobs-into-holes manner. Our binding assay showed that mutations of these nonpolar residues abolished binding to myosin-X, suggesting that the nonpolar interactions are critical for binding (Figure 3D).

In addition to these intimate nonpolar interactions, some polar residues contribute to define the register of the αP3 helix on the groove. Notably, DCC Gln1438 forms a hydrogen bond to the main chain of Phe2002 of the β5C strand (Figure 4A). At the C-terminal end of the αP3 helix, three residues (Thr–Gly–Ser) are folded back and form the C-terminal cap of the helix and the hydrogen bonding network involving Lys2034 from the α1C helix (Figure 4B). This Lys residue forms a salt bridge with Glu1756 from subdomain A so as to bridge the cleft between subdomains A and C. In addition, Lys2031 of the α1C helix forms a hydrogen bond to the main chain of the β4A strand of subdomain A. These inter-subdomain interactions result in stabilization of the mutual position and orientation of the two subdomains and the side-chain conformation of Lys2034. In contrast to the wealth of interactions involving the αP3 helix, the αP3′ helix does not participate in direct interactions with the myosin-X FERM domain. In fact, mutation of two conserved residues (Tyr1420 and Glu1421) of the αP3′ helix does not affect myosin-X binding (Figure 3D).

In summary, DCC binding to the myosin-X FERM domain is predominantly mediated by nonpolar interactions with some critical polar interactions, and the nonpolar and polar residues that participate in the interaction are conserved in DCC and neogenin, indicating similar binding of myosin-X to the neogenin P3 helix (Figure 3B).

Local induced-fit structural changes in myosin-X

It would be of interest to determine if structural changes are induced in the MyTH4–FERM cassette with cargo binding. Our crystal structure of the free form contains two crystallographically independent MyTH4–FERM cassettes. These two cassettes display essentially the same structure with a small overall r.m.s. deviation (1.1 Å). Superimposition of the DCC-bound structure on the free MyTH4–FERM cassette

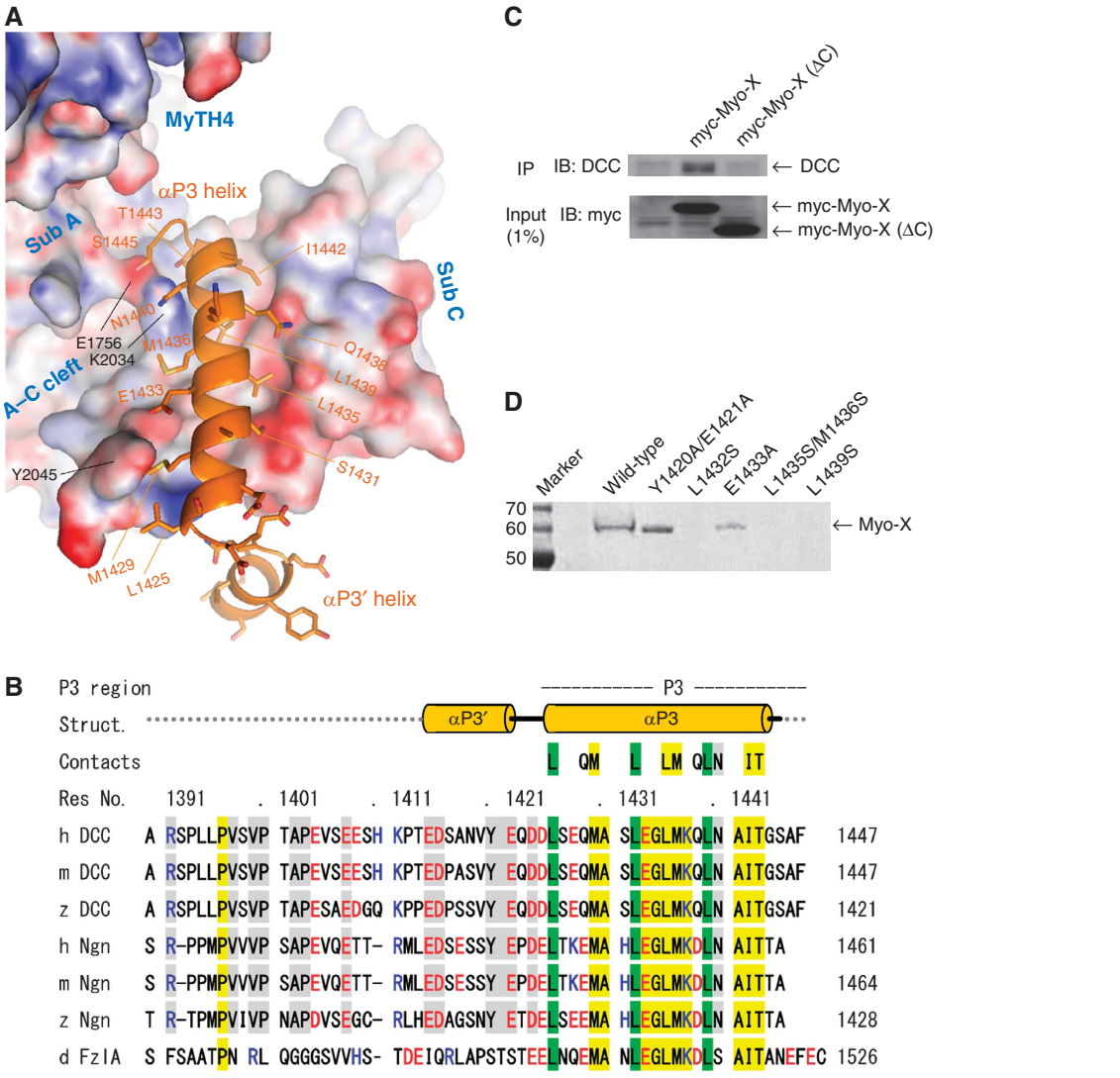

Figure 3 DCC–FERM interactions. (**A**) The DCC P3 peptide docked into the groove of FERM subdomain C. The MyTH4–FERM domain is shown as electrostatic potential surfaces as in Figure 2B. The salt bridge between Glu1756 and Lys2034 bridges the cleft (A–C cleft) between subdomain A (Sub A) and subdomain C (Sub C). (**B**) Sequence alignment of DCC P3 peptide with related receptor C-terminal peptides. The netrin receptors are DCC, Neogenin (Ngn) and Frazzled_A (FzlA). Conserved residues are highlighted in yellow (conserved in all members) and grey (conserved in DCC and neogenin). Heptad repeat residues are highlighted in green. The P3 region (Kolodziej *et al*, 1996) is indicated at the top. Residues that make direct contact with myosin-X are summarized (Contacts). In our current model of the human DCC P3 peptide, 24 N-terminal residues (1390–1413) and 2 C-terminal residues (1446–1447) are missing (indicated with dotted lines) due to poor electron density. (**C**) Direct interactions between the myosin-X MyTH4–FERM cassette and DCC in cells. Co-immunoprecipitation of myosin-X and DCC from HEK293T cells in a manner dependent on subdomain C of the FERM domain. Myc–Myo-X (residues 1486–2058) contains the myc-tagged full-length MyTH4–FERM cassette and myc–Myo-X(ΔC) (residues 1486–1954) lacks subdomain C of the FERM domain. Cell lysates were incubated with anti-myc antibodies to immunoprecipitate the myc–Myo-X–DCC complex, resolved on SDS–PAGE and then immunoblotted with antibodies against myc or DCC. One percent of the input was included in the blot to indicate the amount of relevant proteins. (**D**) Effect of mutations of the DCC P3 peptide on myosin-X binding. Pull-down binding assays of mutated DCC P3 peptides with the myosin-X MyTH4–FERM cassette (Myo-X) were performed with mutations of the αP3′ helix (Tyr1420 and Glu1421) and αP3 helix (Leu1432, Glu1433, Leu1435, Met1436 and Leu1439). Eluted samples were analysed by SDS–PAGE.

structure shows a similar small overall r.m.s. deviation (1.1 Å) (Supplementary Figure S4). Thus, DCC binding induces no significant changes to the overall conformation of the cassette. However, a notable local conformational change was found in subdomain C that directly binds to the DCC peptide. Compared with the free form, the β5C strand is lifted from the α1C helix so as to enlarge the groove width to accommodate the DCC αP3 helix by ∼2 Å (Figure 4A). This induced-fit conformational change is induced by three key cooperative events; formation of a direct hydrogen bond between DCC Gln1438 and the main chain of Phe2002, flipping over of the Phe2002 side chain by ∼90°, which results in it being sandwiched between two nonpolar residues (Leu1435 and Leu1439) from the DCC αP3 helix, and a shift of the β5C strand to produce a nonpolar hole to accommodate the DCC Ile1442 side chain (Figure 3A). The side-chain rotamer transition of Phe2002 may be correlated to the rotamer transition of Val1980, which is relatively remote (∼5.3 Å) from Phe2002 (Figure 4A). These observations imply that subdomain C possesses conformational pliability

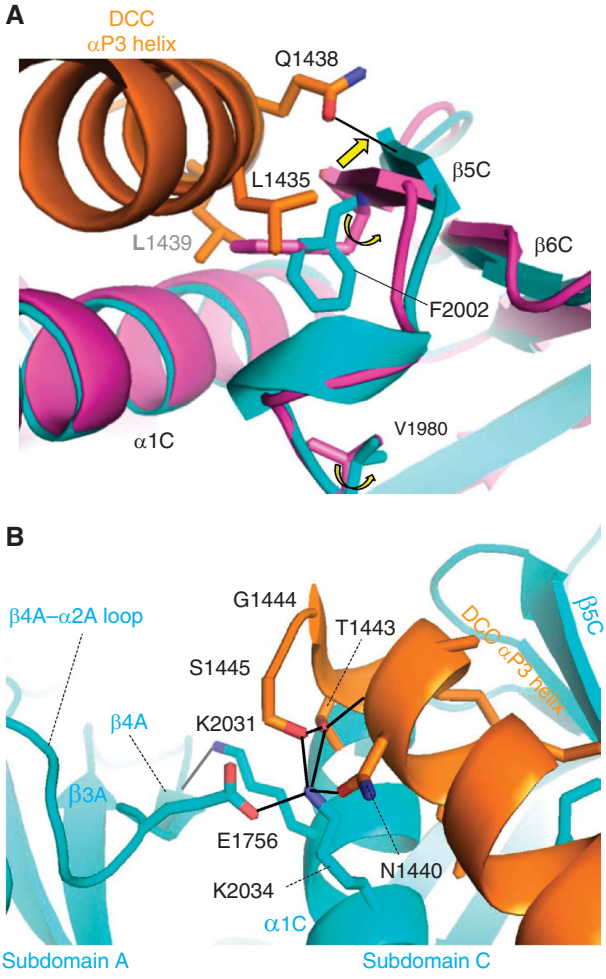

Figure 4 Close-up views of the DCC–myosin-X FERM domain interactions. (**A**) At the middle of the αP3 helix (orange), DCC Gln1438 forms a hydrogen bond with the main chain of myosin-X Phe2002 from the β5C strand of subdomain C, which may contribute to lifting of the strand and result in enlargement of the groove. The DCC-bound form (cyan) is superimposed on the free form (magenta). (**B**) At the C-terminal end of the αP3 helix, three DCC residues (Asn1440, Thr1443 and Ser1445) participate in the hydrogen bonding network formed by multiple hydrogen bonds (solid lines) and the salt bridge between Glu1756 from subdomain A and Lys2034 from subdomain C.

given its intra-domain network of side-chain packing and atomic contacts.

Myosin-X–microtubule interactions

Our microtubule co-sedimentation analyses showed significant co-pelleting of the MyTH4–FERM cassette (Figure 5A), which is consistent with previous studies, which showed that the MyTH4–FERM cassette is sufficient to confer microtubule association (Weber *et al*, 2004). Microtubules possess negatively charged surfaces, predominantly due to ~20 residues of the C-terminal acidic tail, which contains glutamic acid clusters. As our structure reveals a positively charged patch on the MyTH4 domain surface, we supposed that the negatively charged C-terminal tails of tubulin may have a key role in the binding to myosin-X. Using tubulin peptides encompassing the C-terminal acidic tails, our pull-down assays indeed showed that the MyTH4–FERM cassette binds both the C-terminal acidic tail peptides of α- and β-tubulins (Figure 5B). Next, we examined the effect of mutations introduced into the positively charged patch of the MyTH4 domain on binding to tubulin acidic tails. MyTH4 Lys1647 and Lys1650 are located at the centre of the positively charged patch and are expected to have a key role in tubulin binding. Charge-reversal double mutation (K1647D/K1650D) of these basic residues abolished binding to the β2B-tubulin C-terminal tail peptide, while mutation (F2002K) of nonpolar residue Phe2002 of the groove of FERM subdomain C to a polar residue (Lys) had no effect on binding to the tubulin tail (Figure 5C, left panel). Unlike tubulin tail binding, the F2002K mutation of subdomain C abolished DCC binding, but the K1647D/K1650D mutation exhibited only a slight reduction in DCC binding (Figure 5C, right panel). Co-sedimentation experiments also supported this notion that the K1647D/K1650D mutation interferes with co-pelleting of the MyTH4–FERM domain with microtubules but the F2002K mutation causes no interference (Figure 5D). Thus, DCC- and tubulin tail-binding sites are present at different locations within the MyTH4 and FERM domains.

Since these two binding sites are relatively close and positioned at the same side of the molecular surface, we speculated that binding at one site may interfere with binding at the other site. Interestingly, our competition binding assay showed that binding to the tubulin acidic tail peptide is reduced by addition of the DCC P3 peptide (Figure 5E), and co-sedimentation experiments showed that DCC peptide interferes with co-pelleting of the MyTH4–FERM domain with microtubules in a dose-dependent manner (Figure 5F). This dose-dependent competition was not observed if we employed the mutated (F2002K) MyTH4–FERM cassette that fails to bind the DCC peptide (data not shown). All these results suggest interference between microtubule- and DCC-binding events.

Myosin-X–integrin β interactions

Our pull-down assays with the integrin β5 cytoplasmic peptide (residues 743–799) showed binding to the myosin-X MyTH4–FERM cassette (Figure 5G), which is consistent with the previous study which shows that the FERM domain is sufficient to confer binding to the integrin β5 cytoplasmic peptide and mutation of the integrin β5 NPXY motif blocks binding (Zhang *et al*, 2004). This binding is obstructed by addition of the DCC P3 peptide in a dose-dependent manner (Figure 5G), which is coincident with an assumption that the integrin β5 peptide containing the NPXY motif binds the subdomain C groove formed by the α1C helix and the β5C strand in a similar manner to its binding to the talin FERM domain (Wegener *et al*, 2007). Like DCC, integrin β5 interferes microtubule binding, whereas the interference is relatively weaker than DCC (Figure 5H).

Discussion

We have provided the first structures of the MyTH4–FERM cassette in the free and cargo-bound forms. These structures together with the biochemical analyses allow us to delineate the mechanisms that account for the two modes of cargo and microtubule recognition. Of the 37 different types of myosins identified displaying different domain combinations, MyTH4–FERM-containing myosins appear in several species

(Richards and Cavalier-Smith, 2005). Vertebrates possess three conserved MyTH4–FERM-containing myosins, VII, X and XV. Although *Drosophila* is thought to lack myosin-X (Berg *et al*, 2001; Foth *et al*, 2006), the DCC P3 helix is well conserved in frazzled, which encodes a *Drosophila* member of the DCC immunoglobulin subfamily and is required for CNS and motor axon guidance (Kolodziej *et al*, 1996) (Figure 3B). The myosin assigned as myosin-XV may function as myosin-X.

Recently, DCC has been suggested to mediate local translation in neurons by anchoring components of the translational machinery such as ribosome subunits at growth cones and dendrites (Tcherkezian *et al*, 2010). The machinery-binding site of DCC is located at the juxtamembrane P1 region, which is separated from the C-terminal P3 helix by more than 250 residues thought to form a random coil. In fact, the P3 region also exists as a random coil in the free state (Supplementary Figure S5). The DCC cytoplasmic long tail may function as a molecular glue for secondary cargo binding.

In our structure, the MyTH4 domain has no direct contacts with the DCC peptide, in spite of the yeast two-hybrid assay which demonstrated full DCC-binding affinity to the complete MyTH4–FERM cassette but weaker binding affinity to the isolated FERM domain (Zhu *et al*, 2007). We speculated that the MyTH4 domain is necessary for folding and/or maintaining the stable structure of the FERM domain. In fact, we experienced difficulties in expressing isolated MyTH4 or FERM domains in a stable form in bacteria as previously mentioned (Weber *et al*, 2004). This seems to be in line with our observation of rigidity in the overall structure of the MyTH4–FERM cassette, which exhibits no significant conformational changes in the free and DCC-bound states or in different crystal packing environments.

An unexpected finding related to the DCC αP3 helix that was docked into the groove between the β5C strand and the α1C helix of subdomain C of the myosin-X FERM domain (Figure 3A). In sharp contrast to this α-helix groove docking (Figure 6A), binding partners of ERM proteins have been shown to bind this groove of FERM domains by forming an additional anti-parallel β–β association with the β5C strand (Hamada *et al*, 2003; Takai *et al*, 2007, 2008; Terawaki *et al*, 2007; Mori *et al*, 2008) (Figure 6B). In these structures, binding partners such as adhesion molecule ICAM-2, CD43 and PSGL-1 form a short β strand for association with the β5C strand and a 1-turn 3_{10} helix for docking into the groove, and preserve the sequence motif Motif-1α (RxxTYxVxxA, where x stands for any amino-acid residue) (Hamada *et al*, 2003; Takai *et al*, 2007, 2008) (Figure 6B and E). Another adhesion molecule CD44 and a membrane-associated protease NEP preserve the Motif-1β conserved sequence Ile-Asn (IN), and form a short β strand followed by a reverse turn (Terawaki *et al*, 2007; Mori *et al*, 2008). These binding motifs differ from the DCC/neogenin motif that forms the P3 α-helix. Compared with radixin subdomain C, myosin-X possesses a shorter β5C strand (4 residues versus 6 residues of radixin) and shorter α1C helix (5 turns versus 6 turns of radixin), and these are loosely associated to form a larger groove for α-helix accommodation, given the absence of bulky nonpolar residues at the groove surface (Figure 6F).

ERM proteins bind the Na^+/H^+ exchanger regulatory factor-1, 2 (NHERF-1 and -2), which are key cytoplasmic proteins involved in the anchoring of ion channels and receptors to the actin cytoskeleton through binding to ERM proteins. These adaptor proteins preserve FERM-binding Motif-2 (MDWxxxxx(L/I)Fxx(L/F)) and form an α-helix that docks into the groove formed by the β-sandwich loops of subdomain C (Terawaki *et al*, 2006), which displays no similarity to the DCC/neogenin P3 motif (Figure 6C). The myosin-X FERM domain lacks the PtdIns(4,5)P_2-binding site found in the radixin FERM domain as previously described (Figure 6D).

It was one of the most exciting findings in cell biology of cytoskeletons that myosin-X has the ability to function as a motorized link between actin filaments and microtubules in spindle assembly during meiosis (Weber *et al*, 2004; Toyoshima and Nishida, 2007; Woolner *et al*, 2008). However, to date, only a single report of *Xenopus* myosin-X has shown the direct binding of myosin-X to microtubules (Weber *et al*, 2004). Our present studies confirmed that result in a mammalian myosin-X but also revealed that at least the major part of the novel myosin-X–microtubule interaction is mediated by the MyTH4 domain and the C-terminal acidic tails of tubulins. Interestingly, these acidic tails of αβ-tubulins are also collectively referred to as E-hooks, which interact with the kinesin K-loop for processive motor movement (Okada and Hirokawa, 2000; Hirokawa *et al*, 2009). It is well known that α-tubulin acidic tails possess a terminal tyrosine residue at the C-terminus, which is recognized by the CAP-Gly domains of microtubule-binding proteins such as CLIP-170 (Honnappa *et al*, 2006; Mishima *et al*, 2007). The MyTH4–FERM cassette has no homologous region to the CAP-Gly domain and binds both α- and β-tubulin acidic tails.

We showed that the interactions of the MyTH4–FERM domain with microtubules and DCC are mutually exclusive, in spite of the fact that the binding sites are not overlapping. This is particularly important as myosin-X is now reported to have several different binding partners, implying that under different cellular conditions, a different subset of proteins may be associated with myosin-X. It is noteworthy that integrin binding also interferes microtubule binding. We speculate that the primary motor function carrying cargos and the linker function linking an actin filament and a microtubule are two alternative functions of myosin-X.

At present, it is unclear how the interference between tubulin tail and DCC P3 binding occurs, although the C-terminal flexible region of the DCC αP3 helix may interfere with tubulin tail binding to the MyTH4 domain (Supplementary Figure S6). Our present data suggest no significant changes in the overall structure of the MyTH4–FERM cassette on DCC binding. However, it is possible that the acidic tail or microtubule bindings may cause some induced-fit changes in the overall structure. We also speculated that negatively charged residues of the N-terminal flanking region of the DCC P3 peptide may cause electrostatic repulsion with the tubulin acidic tails and the negatively charged surfaces of microtubules.

Recently, the crystal structure of a fusion protein of the myosin-X MyTH4–FERM cassette (human residues 1503–2047) and the DCC P3 peptide (rat 1409–1445) at 2.5 Å resolution has appeared (Wei *et al*, 2011). The fusion protein contains an artificial covalent link between the C-terminus of the subdomain C α1C helix and the N-terminus of the DCC peptide. Compared with our structure, the MyTH4–FERM cassette fused to the DCC P3 peptide displays a relatively

large r.m.s. deviation (1.9 Å) of the overall structures (Supplementary Figure S7A). This unexpectedly large deviation is due to a change in orientation of subdomain C relative to subdomains A and B with an ~5° rotation. Contrary to the overall structures, each FERM subdomain and the MyTH4 domain exhibit relatively small r.m.s. deviations (~1 Å). Like our structure, the fused DCC peptide binds subdomain C with the DCC αP3 helix docked into the subdomain C groove. Side-chain packing at the groove involving conserved nonpolar residues is similar in the two complexes. Nevertheless, superimposition of subdomain C reveals notable local conformational deviations in this subdomain and the bound DCC peptide (Supplementary Figure S7B). Compared with our DCC peptide, the αP3′ helix of the fused DCC peptide is moved by 4.5 Å away from the α1C helix, while the C-terminal region of the α1C helix is shifted away from the DCC αP3′ helix. These movements seem to be induced by the artificial covalent link, which exhibits high mobility with high-temperature factors and seems to push these helices away from each other. These movements result in looser helix packing between the N-terminal region of the α1C helix and the C-terminal region of the αP3 helix of the fused protein.

The most prominent differences are found in polar interactions. In our complex, Lys2034 from the α1C helix has a central role in forming the hydrogen bonding network involving DCC residues (Asn1440, Thr1443 and Ser1445) from the C-terminal end of the αP3 helix (Figure 4B). This network is absent in the fused protein and, instead, Lys2031 forms a single hydrogen bond with Ser1445 (Supplementary Figure S7C). This difference is caused by side-chains rearrangement, which is induced by reorientation of subdomain C, which

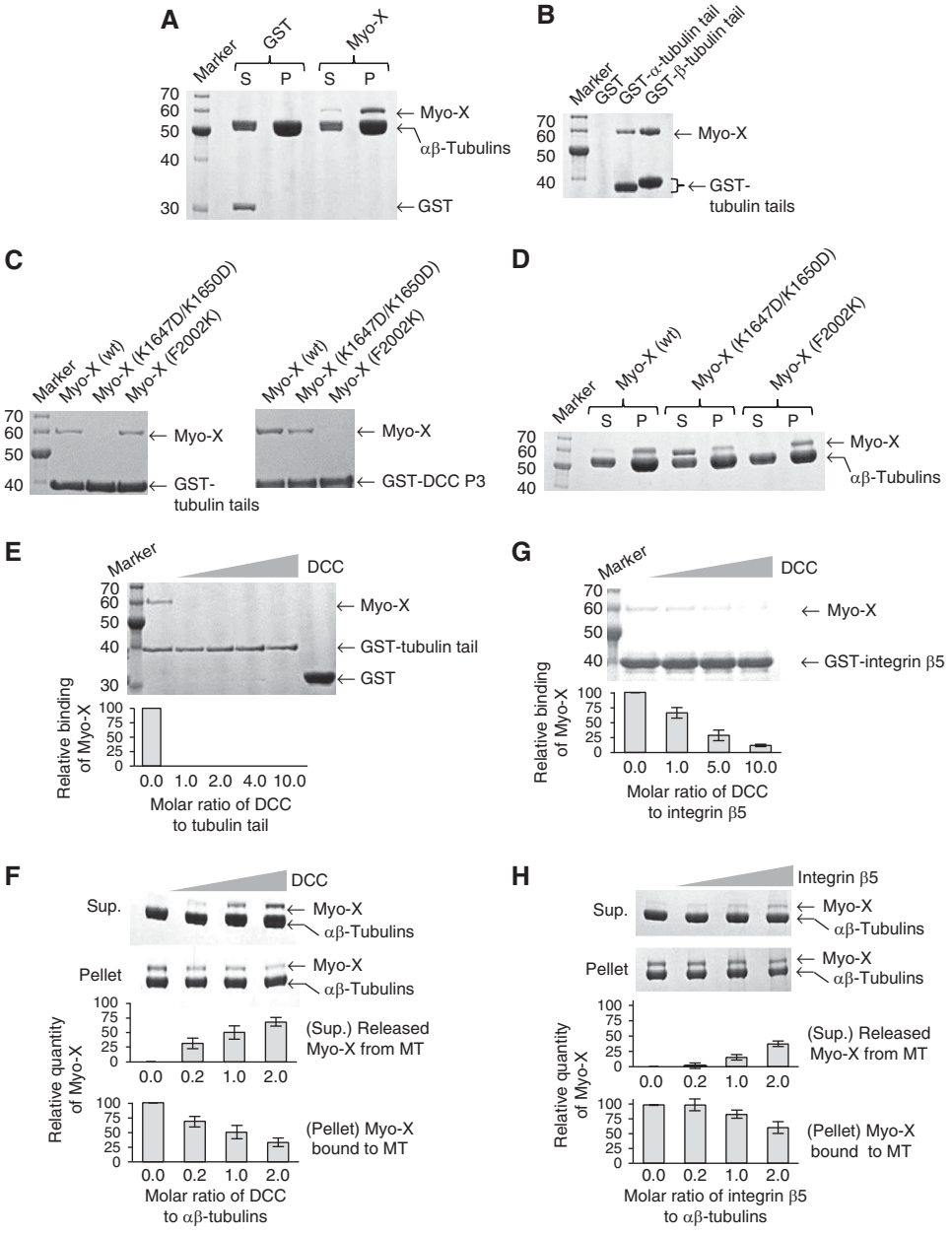

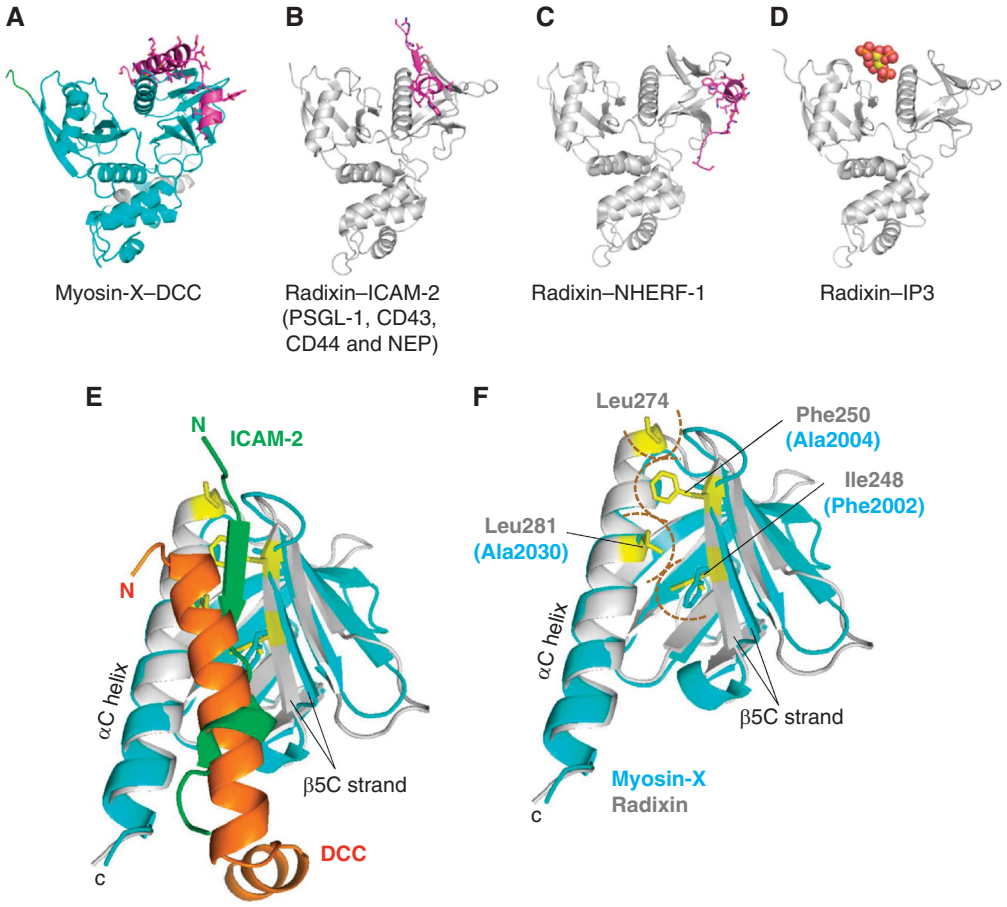

Figure 6 Peptide recognition by FERM domains. Comparison of complex structures of the myosin-X and radixin FERM domains bound to their binding partners. (**A**) The FERM domain of the MyTH4–FERM cassette bound to the DCC P3 peptide of the current structure. (**B**) The radixin–ICAM-2 complex (1J19) exhibits the prototypic binding mode of adhesion molecule recognition by β–β association. A similar binding mode (Motif-1α recognition) is found in both the radixin–PSGL-1 (2EMT) and radixin–CD43 (2EMS) complex structures. The radixin–CD44 (2ZPY) and radixin–NEP (2YVC) complexes also display this binding mode with the modified recognition motif Motif-1β. (**C**) The radixin–NHERF complex (2D10) displays the second class of binding mode with the NHERF peptide docked into the β-sandwich loops. (**D**) The radixin–IP3 complex (1GC6) reveals the PtdIns(4,5)P_2-binding site between subdomains A and C. (**E**) Superimposition of DCC P3 (orange) and ICAM-2 (green) peptides bound to the myosin-X (cyan) and radixin (grey) FERM domains, respectively. The ICAM-2 peptide forms a short β strand followed by a 1-turn 3_{10} helix. (**F**) Superimposition of the myosin-X (cyan) and radixin (grey) FERM domains bound to DCC P3 and ICAM-2 peptides, respectively. The bound peptides are omitted for clarity. Nonpolar residues of the radixin FERM domain are highlighted as stick models (yellow).

Figure 5 Myosin-X MyTH4–FERM cassette interactions with microtubule, DCC and integrin. (**A**) Co-sedimentation of microtubules and the myosin-X MyTH4–FERM cassette (Myo-X). The MyTH4–FERM cassette co-sedimented with microtubules in pellets (P) with little remaining in the soluble fraction (S). (**B**) *In vitro* pull-down binding assays with GST-fused C-terminal tail peptides of α- and β-tubulins. Purified MyTH4–FERM cassette and GST-fused α1A or β2B-tubulin peptide were mixed in 20 mM Tris–HCl (pH 8.0), 50 mM NaCl and 1 mM DTT and incubated at 4°C for 30 min, followed by incubation with glutathione-Sepharose 4B at 4°C for 10 min. After washing five times, proteins were eluted with 20 mM glutathione in 50 mM Tris–HCl buffer (pH 8.0) containing 150 mM NaCl and then subjected to SDS–PAGE. (**C**) Tubulin tail binding to the MyTH4 domain and the DCC P3 peptide binding to the FERM domain. Pull-down assay with the wild-type myosin-X MyTH4–FERM cassette (Myo-X (wt)) shows binding to the GST-fused C-terminal acidic tail peptide of β2B-tubulin (GST-tubulin tail) but the K1647D/K1650D mutation abolished binding (Myo-X (K1647D/K1650D)). The F2002K mutation had no effect on tubulin tail binding (Myo-X (F2002K)). On the other hand, the charge-reversal mutation only weakly affected binding to the GST-DCC P3 peptide and the nonpolar to polar mutation of subdomain C abolished the binding. (**D**) Microtubules bind the MyTH4 but not the FERM domain. Microtubule co-sedimentation experiments with wild-type and mutated myosin-X MyTH4–FERM cassettes used in (**C**). The charge-reversal mutation of the MyTH4 domain abolished or reduced co-sedimentation and the nonpolar to polar mutation of FERM subdomain C had no effect on sedimentation. (**E**) Competition assays show interference between tubulin tail and DCC bindings. Pull-down assay of the myosin-X MyTH4–FERM cassette (Myo-X, 30 μM) with the GST-fused β2B-tubulin peptide was performed in the presence of the DCC P3 peptide (0, 30, 60, 120 and 300 μM). The relative amount of myosin-X pulled down with GST-tubulin in the absence of DCC is shown at the bottom. In this assay, the 30 μM DCC P3 (the 1:1 molar ratio of DCC to MyTH4–FERM) completely abolished tubulin binding. (**F**) Competition assays show interference between microtubule and DCC bindings. Microtubule co-sedimentation experiments with the myosin-X MyTH4–FERM cassette (Myo-X, 4 μM) were performed in the presence of the DCC P3 peptide (0, 4, 20 and 40 μM). The relative ratio of myosin-X to co-precipitated myosin-X with microtubules in the absence of DCC is shown at the bottom. Error bars are standard deviations of each mean value from three independent measurements. (**G**) Competition assays show interference between integrin and DCC bindings. The myosin-X MyTH4–FERM cassette (Myo-X, 10 μM) was pulled down by GST-fused integrin β5 cytoplasmic tail (743–799) in the presence of the DCC P3 peptide (0, 10, 50 and 100 μM). The relative amount of myosin-X pulled down with GST-integrin in the absence of DCC is shown at the bottom with error bars from three independent measurements. (**H**) Competition assays show interference between microtubule and integrin bindings. Microtubule co-sedimentation experiments with the myosin-X MyTH4–FERM cassette (Myo-X, 4 μM) were performed in the presence of the integrin β5 peptide (0, 4, 20 and 40 μM). The relative ratio of myosin-X to co-precipitated myosin-X with microtubules in the absence of DCC is shown at the bottom with error bars from three independent measurements.

shifts away from subdomain A with breaking the inter-subdomain salt bridge between Lys2034 and Glu1756 and the hydrogen bond between Lys2031 and the β4A strand (Figure 4B). Lack of these inter-subdomain interactions destabilizes the hydrogen bonding network, resulting in side-chain rearrangement with destruction of the network. In addition to these movements, the β5C–β6C loop of subdomain C is also moved away from the fused DCC P3 helix and the hydrogen bond involving DCC Gln1438 is missing or neglected probably because of the marginal value (3.4 Å) of the distance. All these differences imply that the DCC binding found in the fused protein may be in a metastable state of binding.

The MyTH4–FERM cassette structure displays a sharp contrast to the recently reported structure of the myosin-VIIa MyTH4–FERM-SH3 cassette bound to cargos the central domain (CEN) of Sans determined at 2.8 Å resolution (Wu *et al*, 2011). The myosin-VIIa MyTH4–FERM cassette is distantly related to the myosin-X MyTH4–FERM cassette with low (∼14%) sequence identity, which is reflected in relatively large deviations of pairwise superimpositions of each subdomains A–C and the MyTH4 domain (r.m.s. deviations ranging from 1.9 to 2.4 Å). Remarkably, superimposition of the overall structures of MyTH4–FERM cassettes of these myosins exhibits a large r.m.s. deviation (6.2 Å for 432 residues) (Supplementary Figure S8). This large deviation is due to reorientations of subdomains B and C, in addition to no structural similarity between the MyTH4 extensions of two myosins. These reorientations could be induced by Sans CEN binding to all three inter-subdomain interfaces formed by subdomains A, B and C. This binding site that is distinct from our DCC-binding site reflects versatility in protein–protein interactions of the FERM domain. Despite these deviations, the MyTH4 domain and subdomain A display a relatively better overlap (the r.m.s. deviation of 2.8 Å), indicating rigidity of the interface between the MyTH4 domain and subdomain C as we discussed with our myosin-X MyTH4–FERM structure. Subdomain arrangements in FERM domains may be more flexibly than we expected before. In fact, the recent structure of the talin FERM domain shows a novel extended conformation (Elliott *et al*, 2010).

In addition to netrin receptors, integrins and microtubules, several reports have suggested other binding partners of myosin-X such as bone morphogenetic protein 6 receptor ALK6 (Pi *et al*, 2007), adhesion molecules such as VE-cadherin (Almagro *et al*, 2010), regulators of actin polymerization such as Mena/VASP (Tokuo and Ikebe, 2004) and spindle-pole assembly factor TPX2 (Woolner *et al*, 2008). The fact that Mena/VASP is a cargo of myosin-X may be related to the reported observation that both the MyTH4 domain and motor function of myosin-X are crucial for actin organization at the leading edge and the promotion of filopodia formation (Bohil *et al*, 2006; Tokuo *et al*, 2007). At present, our sequence analysis failed to detect candidates for myosin-X-binding regions that resemble our DCC P3 peptide or tubulin acidic tails. Lack of sequence similarity between the integrin β5 cytoplasmic peptide and the DCC P3 peptide implies that the myosin-X subdomain C is a protein-binding module of dual or multiple modes. It should be noted that the MyTH4–FERM cassette may possess uncovered binding sites for these binding partners or that these bind other domains of myosin-X.

Materials and methods

Protein expression and purification

A DNA fragment encoding the MyTH4–FERM cassette (residues 1486–2058) of human myosin-X was amplified by the polymerase chain reaction (PCR) and cloned into the pET47b [+] vector

Table I Data collection, phasing and refinement statistics of the human myosin-X MyTH4–FERM domain cassette

	DCC-bound form native	DCC-bound form Se-Met	Free form native
Data collection			
Space group	$P2_1$	$P2_1$	$P2_1$
Cell dimensions			
a, *b*, *c* (Å)	85.2, 49.6, 94.0	85.4, 49.5, 93.4	85.6, 49.3, 158.4
β (deg)	116.7	117.1	93.6
Wavelength (Å)	1.00000	0.97904	0.99458
Resolution (Å)	50–1.9 (1.97–1.90)	50–2.2 (2.28–2.20)	50–2.55 (2.64–2.55)
R_{merge}	0.052 (0.574)	0.068 (0.406)	0.091 (0.482)
$I/\sigma I$	32.1 (2.6)	16.5 (2.4)	18.9 (3.29)
Completeness (%)	99.5 (99.4)	98.8 (97.6)	97.7 (92.2)
Redundancy	3.7 (3.6)	1.9 (1.8)	3.3 (2.9)
Refinement			
Resolution (Å)	50.0–1.9		50–2.55
No. reflections	53 297		40 247
R_{work}/R_{free}	0.215/0.234		0.236/0.282
No. atoms			
Protein	4434		7688
Water	243		94
B-factor (Å^2)			
Protein	39.5		47.4
Water	40.1		33.9
R.m.s. deviations			
Bond lengths (Å)	0.007		0.009
Bond angles (deg)	1.2		1.2

One crystal was used for each data set. Values in parenthesis are for the highest resolution shell.

(Novagen). To prevent degradation, nucleotides encoding residues 1872–1891 of the extra loop were deleted from the plasmid using inverse PCR. The PCR-amplified nucleotides encoding human DCC (residues 1390–1447), α1A-tubulin (399–451), β2B-tubulin (390–445) and integrin β5 cytoplasmic tail (743–799) were cloned into the pET49b [+] vectors (Novagen). All plasmids were verified by DNA sequencing and transformed into *Escherichia coli* strain BL21Star (DE3) (Invitrogen) cells for protein expression.

Protein expression was performed at 20°C in Luria-Bertani medium containing 0.1 mM isopropyl-β-D-thiogalactopyranoside. Cells expressing the myosin-X MyTH4–FERM cassette were harvested, suspended in 20 mM Tris–HCl buffer (pH 8.5) containing 150 mM NaCl and disrupted by sonication. After ultracentrifugation, the supernatant was applied onto a Ni-NTA resin (Qiagen) and treated with HRV3C protease to remove the N-terminal hexahistidine tag. Eluted proteins were further purified by cation exchange (HiTrap SP HP, GE Healthcare) and gel filtration (Superdex 200 pg, GE healthcare) chromatography. For preparation of the DCC P3, tubulin tail and integrin peptides, wet cells expressing proteins were suspended in 20 mM Tris–HCl buffer (pH 8.0) containing 150 mM NaCl and disrupted by sonication. Following ultracentrifugation, the supernatant was purified by glutathione-Sepharose 4B column (GE Healthcare), anion exchange (HiTrap Q HP, GE Healthcare) and gel filtration (Superdex 75 pg, GE Healthcare) chromatography. For crystallization, the GST-fused DCC P3 peptide was treated with HRV3C protease to remove the N-terminal GST tag. Separately purified myosin-X MyTH4–FERM cassette and DCC P3 peptide were mixed and the 1:1 complex was purified using gel filtration chromatography.

For structure determination, protein expression of the selenomethione (SeMet)-labelled MyTH4–FERM cassette was performed in M9 medium containing SeMet under conditions inhibiting the methionine biosynthesis pathway (Doublié, 1997). The expression conditions and purification procedures were the same as those used for the native protein. The purified proteins were verified using matrix-assisted laser desorption/ionization time-of-flight mass spectroscopy (MALDI–TOF-MS; Bruker Daltonics).

Crystallization and data collection

Initial crystallization conditions were screened using a Hydra II Plus One crystallization robot (Matrix Technology) with commercial crystallization-solution kits, JCSG Core Suite I–IV and PACT Suite (Qiagen). The best crystals of the complex between myosin-X MyTH4–FERM cassette and DCC P3 peptide were obtained from solutions containing 5 mg/ml of the complex and reservoir solution containing 100 mM malic acid-MES-Tris (MMT) buffer (pH 8.0) and 2% polyethylene glycol (PEG) 1500 at 20°C. Crystals of the free myosin-X MyTH4–FERM cassette were obtained using reservoir solution containing 10% PEG 8000, 5% MPD and 0.1 M HEPES (pH 7.5) from protein solutions containing the myosin-X MyTH4–FERM cassette and β-tubulin (390–445) in an equimolar ratio (112 μM). These crystals appeared to contain no β-tubulin within the crystals. The crystals obtained were transferred stepwise into a cryoprotective solution containing 30% glycerol (for the MyTH4–FERM/DCC complex) or 25% ethylene glycol (for the MyTH4–FERM cassette) and flash cooled at 100 K. X-ray diffraction data were collected at 100 K on a BL41XU or BL44XU beamline at SPring-8. All data were processed and scaled using *HKL-2000* (Otwinowski and Minor, 1997). The crystal data are summarized in Table I.

Structure determination and refinement

Phases of the complex crystal were calculated by a SAD method using data collected at the peak wavelength of selenium. Selenium positions were located using the program BnP (Weeks *et al*, 2002) and phase refinement by solvent flattening was performed with RESOLVE (Terwilliger, 2004). The built model was refined through alternating cycles using the Coot (Emsley and Cowtan, 2004) and CNS (Brünger *et al*, 1998) programs. The model was refined to 1.9 Å resolution. In the Ramachandran plots using MolProbity (Davis *et al*, 2007), no outliers were flagged. The free form structure of the MyTH4–FERM cassette was determined by the molecular replacement method using the cassette model of the complex structure and refined at 2.55 Å. The refinement statistics are summarized in Table I.

Structure and sequence comparison

Multiple sequence alignments of the MyTH4–FERM cassettes and the netrin receptors were performed by CLUSTALW (Larkin *et al*, 2007). Pairwise structural comparisons were performed using C_α-atom positions by the DALI lite server (Holm and Park, 2000) and structure figures were prepared by PyMOL (http://www.pymol.org/). In the course of the review process of this article, the crystal structures of the tail domains of myosins-X and myosin-VIIa have appeared (Wei *et al*, 2011; Wu *et al*, 2011). The appearance of structures display a similar fold of the MyTH4–FERM cassette seemed to provide a useful opportunity to review our structures, but significant deviations also appeared among these structures (see text).

Analytical ultracentrifugation

Sedimentation velocity ultracentrifugation experiments were performed at 20°C using a Beckman Coulter Optima XLA analytical ultracentrifuge. Purified samples were dissolved in 20 mM Tris buffer (pH 8.5) containing 150 mM NaCl and 5 mM DTT at a sample concentration of 1 mg/ml (14 μM) and then centrifuged at 25 000 r.p.m. The resultant data were analysed using the programs SEDFIT and SEDNTERP.

Binding studies by isothermal titration calorimetric analysis

ITC analysis was conducted using a calorimeter (MicroCal VP-ITC, USA) at 20°C. Purified protein samples were dialysed overnight in buffer containing 20 mM Tris–HCl (pH 8.5) and 150 mM NaCl. Data fitting were performed using the ORIGIN™ software program supplied with the instrument.

Pull-down binding assay

All mutations were produced by site-directed mutagenesis. For *in vitro* pull-down binding assays, the purified myosin-X MyTH4–FERM domain cassette and GST-fusion protein were mixed with a slurry of glutathione-Sepharose 4B and incubated at 4°C. After washing with incubation buffer solution, the eluates were subjected to SDS–PAGE.

Co-sedimentation assay with microtubules

Forty micromolar tubulin heterodimer in 100 mM PIPES (pH 6.9), 1 mM EGTA and 1 mM $MgSO_4$ (PEM buffer) containing 1 mM GTP and 10 μM taxol was polymerized by incubation at 37°C for 20 min. Protein samples were mixed with the polymerized tubulin at a molar ratio of 1:5 (protein sample to tubulin) and the samples were further incubated at 37°C for 20 min. After centrifugation at 14 000 *g* at 4°C for 30 min, the resulting pellets and supernatants were subjected to SDS–PAGE. Bands of myosin-X were analysed by a densitometric analysis for quantitative evaluation of the inhibitory effects by DCC.

Co-immunoprecipitation

HEK293T cells were transiently transfected with cDNA by the calcium phosphate method. Two days after transfection, cells were washed with PBS and lysed with modified RIPA buffer (50 mM Tris–HCl pH 7.4, 150 mM NaCl, 1% NP-40, 0.25% sodium-deoxycholate, 2 mM phenylmethylsulfonyl fluoride and 5 μg/ml leupeptin) and centrifuged at 17 000 *g* for 10 min at 4°C. The supernatants were incubated with anti-myc antibody (MBL, M047-3) for 1 h at 4°C, and immune complexes were then precipitated with protein G-Sepharose 4B (GE Healthcare) for 1 h at 4°C. After washing, the beads with lysis buffer, immunocomplexes were analysed by immunoblot.

Accession codes

Protein Data Bank: The coordinates and structure factors of the human myosin-X MyTH4–FERM cassette and its complex with the DCC P3 peptide have been deposited under accession codes 3AU5 and 3AU4, respectively.

Supplementary data

Supplementary data are available at *The EMBO Journal* Online (http://www.embojournal.org).

Acknowledgements

We thank J Tsukamoto for technical support in performing mass spectroscopy and amino-terminal analyses, and the beamline staffs

of BL41XU of SPring-8 at Harima for technical help with the data collection. This work was supported by a Grant-in-Aid for Scientific Research from the Ministry of Education, Culture, Sports, Science and Technology (MEXT) of Japan on Innovative Area 'Structural Cell Biology' and in part for Scientific Research (A) (to TH), for Young Scientists (to YH) and for Scientific Research (B) (to NI). This work was also supported by a research grant from the Uehara Memorial Life Science Foundation, Japan (to TH). YH is a recipient of a research grant for Young Scientists from the Global COE Program in NAIST (Frontier Biosciences) from MEXT of Japan.

Author contributions: TH conceived and designed the project. YH was responsible for construct design for protein preparation. TH, AT and YH were responsible for execution of protein biochemistry/biophysics, crystallization and data collection. YH solved and refined the complex structures. MT performed *in vivo* assay directed by NI. YH and TH interpreted data and TH wrote the manuscript.

Conflict of interest

The authors declare that they have no conflict of interest.

References

Almagro S, Durmort C, Chervin-Pétinot A, Heyraud S, Dubois M, Lambert O, Maillefaud C, Hewat E, Schaal JP, Huber P, Gulino-Debrac D (2010) The motor protein myosin-X transports VE-cadherin along filopodia to allow the formation of early endothelial cell-cell contacts. *Mol Cell Biol* **30:** 1703–1717

Berg JS, Cheney RE (2002) Myosin-X is an unconventional myosin that undergoes intrafilopodial motility. *Nat Cell Biol* **4:** 246–250

Berg JS, Derfler BH, Pennisi CM, Corey DP, Cheney RE (2000) Myosin-X, a novel myosin with pleckstrin homology domains, associates with regions of dynamic actin. *J Cell Sci* **113:** 3439–3451

Berg JS, Powell BC, Cheney RE (2001) A millennial myosin census. *Mol Biol Cell* **12:** 780–794

Bohil AB, Robertson BW, Cheney RE (2006) Myosin-X is a molecular motor that functions in filopodia formation. *Proc Natl Acad Sci USA* **103:** 12411–12416

Brünger AT, Adams PD, Clore GM, DeLano WL, Gros P, Grosse-Kunstleve RW, Jiang JS, Kuszewski J, Nilges M, Pannu NS, Read RJ, Rice LM, Simonson T, Warren GL (1998) Crystallography & NMR system: a new software suite for macromolecular structure determination. *Acta Crystallogr D* **54:** 905–921

Chan SS, Zheng H, Su MW, Wilk R, Killeen MT, Hedgecock EM, Culotti JG (1996) UNC-40, a C. elegans homolog of DCC (Deleted in Colorectal Cancer), is required in motile cells responding to UNC-6 netrin cues. *Cell* **87:** 187–195

Davis IW, Leaver-Fay A, Chen VB, Block JN, Kapral GJ, Wang X, Murray LW, Arendall III WB, Snoeyink J, Richardson JS, Richardson DC (2007) MolProbity: all-atom contacts and structure validation for proteins and nucleic acids. *Nucleic Acids Res* **35:** W375–W383

Doublié S (1997) Preparation of selenomethionyl proteins for phase determination. *Methods Enzymol* **276:** 523–530

Edwards SD, Keep NH (2001) The 2.7 Å crystal structure of the activated FERM domain of moesin: an analysis of structural changes on activation. *Biochemistry* **40:** 7061–7068

Elliott PR, Goult BT, Kopp PM, Bate N, Grossmann JG, Roberts GC, Critchley DR, Barsukov IL (2010) The Structure of the talin head reveals a novel extended conformation of the FERM domain. *Structure* **18:** 1289–1299

Emsley P, Cowtan K (2004) Coot: model-building tools for molecular graphics. *Acta Crystallogr D* **60:** 2126–2132

Foth BJ, Goedecke MC, Soldati D (2006) New insights into myosin evolution and classification. *Proc Natl Acad Sci USA* **103:** 3681–3686

Hamada K, Shimizu T, Matsui T, Tsukita S, Hakoshima T (2000) Structural basis of the membrane-targeting and unmasking mechanisms of the radixin FERM domain. *EMBO J* **19:** 4449–4462

Hamada K, Shimizu T, Yonemura S, Tsukita S, Tsukita S, Hakoshima T (2003) Structural basis of adhesion-molecule recognition by ERM proteins revealed by the crystal structure of the radixin-ICAM-2 complex. *EMBO J* **22:** 502–514

Hirokawa N, Nitta R, Okada Y (2009) The mechanisms of kinesin motor motility: lessons from the monomeric motor KIF1A. *Nat Rev Mol Cell Biol* **10:** 877–884

Holm L, Park J (2000) DaliLite workbench for protein structure comparison. *Bioinformatics* **16:** 566–567

Honnappa S, Okhrimenko O, Jaussi R, Jawhari H, Jelesarov I, Winkler FK, Steinmetz MO (2006) Key interaction modes of dynamic +TIP networks. *Mol Cell* **23:** 663–671

Isakoff SJ, Cardozo T, Andreev J, Li Z, Ferguson KM, Abagyan R, Lemmon MA, Aronheim A, Skolnik EY (1998) Identification and analysis of PH domain-containing targets of phosphatidylinositol 3-kinase using a novel *in vivo* assay in yeast. *EMBO J* **17:** 5374–5387

Keino-Masu K, Masu M, Hinck L, Leonardo ED, Chan SS, Culotti JG, Tessier-Lavigne M (1996) Deleted in Colorectal Cancer (DCC) encodes a netrin receptor. *Cell* **87:** 175–185

Kolodziej PA, Timpe LC, Mitchell KJ, Fried SR, Goodman CS, Jan LY, Jan YN (1996) frazzled encodes a Drosophila member of the DCC immunoglobulin subfamily and is required for CNS and motor axon guidance. *Cell* **87:** 197–204

Larkin MA, Blackshields G, Brown NP, Chenna R, McGettigan PA, McWilliam H, Valentin F, Wallace IM, Wilm A, Lopez R, Thompson JD, Gibson TJ, Higgins DG (2007) Clustal W and Clustal X version 2.0. *Bioinformatics* **23:** 2947–2948

Lohi O, Poussu A, Mao Y, Quiocho F, Lehto VP (2002) VHS domain—a longshoreman of vesicle lines. *FEBS Lett* **513:** 19–23

Mao Y, Nickitenko A, Duan X, Lloyd TE, Wu MN, Bellen H, Quiocho FA (2000) Crystal structure of the VHS and FYVE tandem domains of Hrs, a protein involved in membrane trafficking and signal transduction. *Cell* **100:** 447–456

Mishima M, Maesaki R, Kasa M, Watanabe T, Fukata M, Kaibuchi K, Hakoshima T (2007) Structural basis for tubulin recognition by cytoplasmic linker protein 170 and its autoinhibition. *Proc Natl Acad Sci USA* **104:** 10346–10351

Misra S, Puertollano R, Kato Y, Bonifacino JS, Hurley JH (2002) Structural basis for acidic-cluster-dileucine sorting-signal recognition by VHS domains. *Nature* **415:** 933–937

Mizuno E, Kawahata K, Kato M, Kitamura N, Komada M (2003) STAM proteins bind ubiquitinated proteins on the early endosome via the VHS domain and ubiquitin-interacting motif. *Mol Biol Cell* **14:** 3675–3689

Mori T, Kitano K, Fukami Y, Terawaki S, Hakoshima T (2008) Structural properties of the cytoplasmic tail of adhesion molecule CD44 and its binding to FERM proteins. *J Biol Chem* **283:** 29602–29612

O'Connell CB, Tyska MJ, Mooseker MS (2007) Myosin at work: motor adaptations for a variety of cellular functions. *Biochim Biophys Acta* **1773:** 615–630

Okada Y, Hirokawa N (2000) Mechanism of the single-headed processivity: diffusional anchoring between the K-loop of kinesin and the C terminus of tubulin. *Proc Natl Acad Sci USA* **97:** 640–645

Otwinowski Z, Minor W (1997) Processing of X-ray diffraction data collected in oscillation mode. *Methods Enzymol* **276:** 307–326

Pearson MA, Reczek D, Bretscher A, Karplus PA (2000) Structure of the ERM protein moesin reveals the FERM domain fold masked by an extended actin binding tail domain. *Cell* **101:** 259–270

Pi X, Ren R, Kelley R, Zhang C, Moser M, Bohil AB, Divito M, Cheney RE, Patterson C (2007) Sequential roles for myosin-X inBMP6-dependent filopodial extension, migration, and activation of BMP receptors. *J Cell Biol* **179:** 1569–1582

Ren X, Hurley JH (2010) VHS domains of ESCRT-0 cooperate in high-avidity binding to polyubiquitinated cargo. *EMBO J* **29:** 1045–1054

Richards TA, Cavalier-Smith T (2005) Myosin domain evolution and the primary divergence of eukaryotes. *Nature* **436:** 1113–1118

Shiba T, Takatsu H, Nogi T, Matsugaki N, Kawasaki M, Igarashi N, Suzuki M, Kato R, Earnest T, Nakayama K, Wakatsuki S (2002) Structural basis for recognition of acidic-cluster dileucine sequence by GGA1. *Nature* **415:** 937–941

Shimizu T, Seto A, Maita N, Hamada K, Tsukita S, Tsukita S, Hakoshima T (2002) Structural basis for neurofibromatosis

Type 2: crystal structure of the Merlin FERM domain. *J Biol Chem* **277:** 10332–10336

Smith WJ, Nassar N, Bretscher A, Cerione RA, Karplus PA (2003) Structure of the active N-terminal domain of Ezrin. Conformational and mobility changes identify keystone interactions. *J Biol Chem* **278:** 4949–4956

Sousa AD, Cheney RE (2005) Myosin-X: a molecular motor at the cell's fingertips. *Trends Cell Biol* **15:** 533–539

Takai Y, Kitano K, Terawaki S, Maesaki R, Hakoshima T (2007) Structural basis of PSGL-1 binding to ERM proteins. *Genes Cell* **12:** 1329–1338

Takai Y, Kitano K, Terawaki S, Maesaki R, Hakoshima T (2008) Structural basis of the cytoplasmic tail of adhesion molecule CD43 and its binding to ERM proteins. *J Mol Biol* **381:** 634–644

Tcherkezian J, Brittis PA, Thomas F, Roux PP, Flanagan JG (2010) Transmembrane receptor DCC associates with protein synthesis machinery and regulates translation. *Cell* **141:** 632–644

Terawaki S, Kitano K, Hakoshima T (2007) Structural basis for type II membrane protein binding by ERM proteins revealed by the radixin-neutral endopeptidase 24.11 (NEP) complex. *J Biol Chem* **282:** 19854–19861

Terawaki S, Maesaki R, Hakoshima T (2006) Structural basis of NHERF recognition by ERM proteins. *Structure* **14:** 777–789

Terwilliger T (2004) SOLVE and RESOLVE: automated structure solution, density modification and model building. *J Synchrotron Radiat* **11:** 49–52

Tokuo H, Ikebe M (2004) Myosin X transports Mena/VASP to the tip of fiopodia. *Biochem Biophys Res Commun* **319:** 214–220

Tokuo H, Mabuchi K, Ikebe M (2007) The motor activity of myosin-X promotes actin fiber convergence at the cell periphery to initiate filopodia formation. *J Cell Biol* **179:** 229–238

Toyoshima F, Nishida E (2007) Integrin-mediated adhesion orients the spindle parallel to the substratum in an EB1- and myosin X-dependent manner. *EMBO J* **26:** 1487–1498

Weber KL, Sokac AM, Berg JS, Cheney RE, Bement WM (2004) A microtubule-binding myosin required for nuclear anchoring and spindle assembly. *Nature* **431:** 325–329

Weeks CM, Blessing RH, Miller R, Mungee R, Potter SA, Rappleye J, Smith GD, Xu H, Furey W (2002) Towards automated protein structure determination: BnP, the SnB-PHASES interface. *Z Kristallogr* **217:** 686–693

Wegener KL, Partridge AW, Han J, Pickford AR, Liddington RC, Ginsberg MH, Campbell ID (2007) Structural basis of integrin activation by talin. *Cell* **128:** 171–182

Wei Z, Yan J, Lu Q, Pan L, Zhang M (2011) Cargo recognition mechanism of myosin X revealed by the structure of its tail MyTH4-FERM tandem in complex with the DCC P3 domain. *Proc Natl Acad Sci USA* **108:** 3572–3577

Woolner S, Bement WM (2009) Unconventional myosins acting unconventionally. *Trends Cell Biol* **19:** 245–252

Woolner S, O'Brien LL, Wiese C, Bement WM (2008) Myosin-10 and actin filaments are essential for mitotic spindle function. *J Cell Biol* **182:** 77–88

Wu L, Pan L, Wei Z, Zhang M (2011) Structure of MyTH4-FERM domains in myosin VIIa tail bound to cargo. *Science* **331:** 757–760

Yu C, Feng W, Wei Z, Miyanoiri Y, Wen W, Zhao Y, Zhang M (2009) Myosin VI undergoes cargo-mediated dimerization. *Cell* **138:** 537–548

Zhang H, Berg JS, Li Z, Wang Y, Lång P, Sousa AD, Bhaskar A, Cheney RE, Strömblad S (2004) Myosin-X provides a motor-based link between integrins and the cytoskeleton. *Nat Cell Biol* **6:** 523–531

Zhu XJ, Wang CZ, Dai PG, Xie Y, Song NN, Liu Y, Du QS, Mei L, Ding YQ, Xiong WC (2007) Myosin X regulates netrin receptors and functions in axonal path-finding. *Nat Cell Biol* **9:** 184–192